

Article

Mapping the Loss of Mt. Kenya's Glaciers: An Example of the Challenges of Satellite Monitoring of Very Small Glaciers

Rainer Prinz ^{1,*} , Armin Heller ², Martin Ladner ^{2,3} , Lindsey I. Nicholson ⁴ and Georg Kaser ⁴

¹ Department of Geography and Regional Science, University of Graz, Heinrichstrasse 36, 8010 Graz, Austria

² Institute of Geography, University of Innsbruck, Innrain 52, 6020 Innsbruck, Austria; armin.heller@uibk.ac.at (A.H.); martin.ladner@uibk.ac.at (M.L.)

³ Austrian Alpine Club, Olympiastrasse 37, 6020 Innsbruck, Austria

⁴ Institute of Atmospheric and Cryospheric Sciences, University of Innsbruck, Innrain 52, 6020 Innsbruck, Austria; lindsey.nicholson@uibk.ac.at (L.I.N.); georg.kaser@uibk.ac.at (G.K.)

* Correspondence: rainer.prinz@uni-graz.at; Tel.: +43-316-380-8296

Received: 31 March 2018; Accepted: 5 May 2018; Published: 11 May 2018



Abstract: Since the last complete glacier mapping of Mt. Kenya in 2004, strong glacier retreat and glacier disintegration have been reported. Here, we compile and present a new glacier inventory of Mt. Kenya to document recent glacier change. Glacier area and mass changes were derived from an orthophoto and digital elevation model extracted from Pléiades tri-stereo satellite images. We additionally explore the feasibility of using freely available imagery (Sentinel-2) and an alternative elevation model (TanDEM-X-DEM) for monitoring very small glaciers in complex terrain, but both proved to be inappropriate; Sentinel-2 because of its too coarse horizontal resolution compared to the very small glaciers, and TanDEM-X-DEM because of errors in the steep summit area of Mt. Kenya. During 2004–2016, the total glacier area on Mt. Kenya decreased by $121.0 \times 10^3 \text{ m}^2$ (44%). The largest glacier (Lewis) lost $62.8 \times 10^3 \text{ m}^2$ (46%) of its area and $1.35 \times 10^3 \text{ m}^3$ (57%) of its volume during the same period. The mass loss of Lewis Glacier has been accelerating since 2010 due to glacier disintegration, which has led to the emergence of a rock outcrop splitting the glacier in two parts. If the current retreat rates prevail, Mt. Kenya's glaciers will be extinct before 2030, implying the cessation of the longest glacier monitoring record of the tropics.

Keywords: glacier monitoring; glacier inventory; satellite remote sensing; Pléiades satellite images; Sentinel-2; TanDEM-X; DEM; Mount Kenya; tropical glacier

1. Introduction

Glaciers act as low pass filters of climate variability [1], and are, therefore, key indicators of climate change [2]. For this reason, glacier monitoring is implemented in the Global Climate/Terrestrial Observing System (GCOS/GTOS) via a Global Hierarchical Observing Strategy (GHOST) [3]. Following the tiers defined in this strategy, long-term observations of glaciers currently demonstrate historically unprecedented global glacier area and mass losses [4], which pose challenges to existing monitoring networks, such as glacier disintegration, increasing debris cover, and complete extinction of glaciers [5]. To keep pace with the rapid ongoing changes, glacier monitoring at appropriate spatial and temporal scales becomes increasingly important [6,7]. Enhanced Earth observing systems facilitate glacier monitoring in most remote areas [8], however, the variations of very small glaciers ($<0.1 \text{ km}^2$) in complex mountainous terrain remain a challenge for detection [9].

The glaciers on Mt. Kenya ($0^\circ 9' \text{ S}$, $37^\circ 18' \text{ E}$) are among the best studied tropical glaciers. Glacier changes have been reported since the late 19th century, including (sub) decadal mappings

from 1934 onwards, and surface mass balance measurements from 1979 to 1996, and from 2010 to 2014 [10–12] (and references therein). The last glacier inventory on Mt. Kenya was carried out in 2004 [13], showing that between 1899 and 2004, the total area of 18 glaciers decreased from 1.64 km² to 0.27 km² (–84%), while 8 glaciers vanished completely [14]. The most recent mapping of the largest glacier (Lewis, Figure 1) was performed in 2010 [15,16], which confirmed the strong retreat rates, indicating that between 1934 and 2010 the glacier lost 90% (79%) of its volume (area) [12]. A climate sensitivity study based on energy balance modelling found that glacier recession since the late 19th century can be primarily attributed to atmospheric drying resulting in reduced cloudiness, snowfall, and albedo [17]. Similar studies proved the climate proxy potential of tropical glaciers [18–20] as they capture climate signals from the tropical mid-troposphere, where our understanding is scarce and controversial [21,22]. Although Mt. Kenya’s glaciers have limited socioeconomic relevance [23], they have the longest record of glacier monitoring in the tropics. Recent reports of substantial glacier changes [24,25] demand an update of Mt. Kenya’s glaciers inventory, offering unique witnessing of the impending deglaciation of an entire massif.

Direct glacier observations on Mt. Kenya ceased in 2014 [24], leaving remote sensing as the only option for a continuous monitoring strategy. In this study, we use very high resolution (0.5 m) satellite images from Pléiades tri-stereo scenes (acquired in 2016), which are processed to an orthophoto and to a digital elevation model (DEM) of the summit area. From the orthophoto, we derive a new glacier inventory of Mt. Kenya and quantify glacier area changes by comparison to the previous inventory, which was derived from the last complete glacier mapping in 2004. For quantifying glacier volume changes, we subtract Lewis Glacier DEMs from 2016 and 2010. Additionally, to explore the capability of available remote sensing data to monitor the changes of Mt. Kenya glaciers, we test the Pléiades orthophoto and DEM against freely available products, like Sentinel-2 satellite images and the TanDEM-X-DEM.



Figure 1. Lewis Glacier above Lewis Tarn seen from its late 19th century lateral moraine on 01 March 2011. Note the steep walls of the two highest peaks of the massif, Batian (5199 m) and Nelion (5188 m), which rise to the upper left corner. Photo credit R. Prinz.

2. Materials and Methods

2.1. Pléiades Tri-Stereo DEM and Orthophoto

The Pléiades system (operated by the Centre National d’Études Spatiales) consists of two identical optical satellites Pléiades 1A and 1B, positioned with a 180° phase shift in a sun-synchronous orbit at 694 km altitude enabling a daily acquisition of any point on Earth. During a single fly

in longitudinal-scan mode (along-track), image triplets (tri-stereo) can be taken in a few seconds in the direction of forward, backward, and near perpendicular (nadir).

Access to the Pléiades scenes was granted via a mapping project of the Austrian Alpine Club (<http://www.gis.tirol/AV.MAP/>). For a new edition of the trekking map of Mt. Kenya six Pléiades tri-stereo images (Table 1) were purchased from Airbus Defense and Space, and serve as terrain and land surface layers. The total map domain covers around 1050 km². In this study, we examine only a subdomain covering the summit area of Mt. Kenya (6.3 km²), representing the same domain as the map of 2004 [13]. The Pléiades acquisition time at Mt. Kenya is around 8:00 UTC (11:00 local time, Table 1). This timing fortunately avoids problems associated with large shadows, as the solar elevation is high at this time, and also issues of clouds, which tend to form from noon onwards following the pronounced diurnal weather cycle in the tropics [17]. The acquisition date at the end of the dry season, is ideal for glacier monitoring as it is generally associated with the minimum extent of seasonal snow cover.

Table 1. Details of the Pléiades tri-stereo primary products used in this study.

Satellite	Imaging Date	Time (UTC)	Global Incidence (°)	Track Incidence Across (°)	Track Incidence Along (°)	Solar Azimuth (°)	Solar Elevation (°)
PHR 1B	21 December 2015	7:58:54	5.62	5.36	1.69	138.3	58.0
PHR 1A	22 February 2016	8:02:30	3.03	−1.91	2.36	130.0	58.0
PHR 1B	4 February 2016	8:02:45	2.94	−2.85	−0.76	124.0	58.2
PHR 1A	17 February 2016	8:02:14	4.99	−3.63	−3.43	116.3	58.5
PHR 1A	17 February 2016	8:02:26	4.07	−3.40	2.24	116.0	59.9
PHR 1B	23 February 2016	8:06:20	12.55	−11.83	−4.29	112.6	61.9

To generate the terrain model, Pléiades tri-stereo images for the entire domain were processed to a DEM (PLE) with ESRI ArcGIS Pro (version 2.01, Environmental Systems Research Institute, Redlands, CA, USA), according to the scheme shown in Figure 2, using no ground control points. Mosaicking overlapping scenes reduced cloud cover. Point clouds resulting from the stereo model builder were filtered for outliers (no noise) to improve the terrain model, which was used for orthorectification of the panchromatic and multispectral images. Applying pansharpening, the images were finally combined to high geometric resolution images. Thus, three orthophotos (forward, backward, and nadir) with no cloud cover in the summit domain and a digital surface model (DSM) at 1 m resolution (UTM WGS84, elevations referring to mean sea level) are available for our purpose (Table 2). Note, because in the summit domain of Mt. Kenya plants do not grow taller than tussock, and there are just a few small huts, there is no difference between the surface elevation and the terrain elevation. Hence, we use the terms DSM and DEM synonymously.

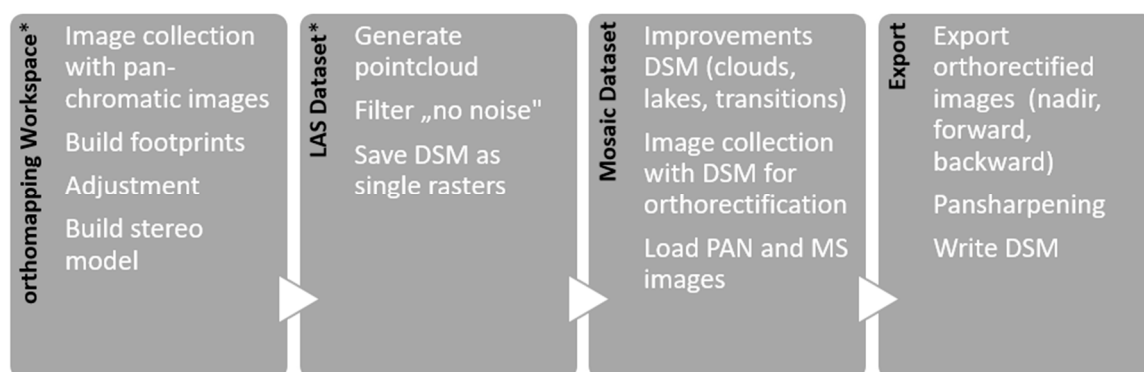


Figure 2. Step-by-step processing of the digital surface model (DSM) and the orthophoto with ESRI ArcGIS Pro 2.01. * calculation step individually per scene.

ESRI provides different matching algorithms for DEM construction, of which we tested two: the semi-global matching (SGM) algorithm [26] and the extended terrain matching (ETM) tool,

a feature-based stereo matching algorithm based on the Harris feature point detector [27]. SGM derives much denser point clouds, but presumably, due to the distortion of the steep terrain, the algorithm introduced artefacts to the DEM matching, which caused invalid results. ETM provided much better results for cartographic purposes than SGM, and was finally used in this study. Figure 3 shows the differences and illustrates the defective results of the SGM algorithm.

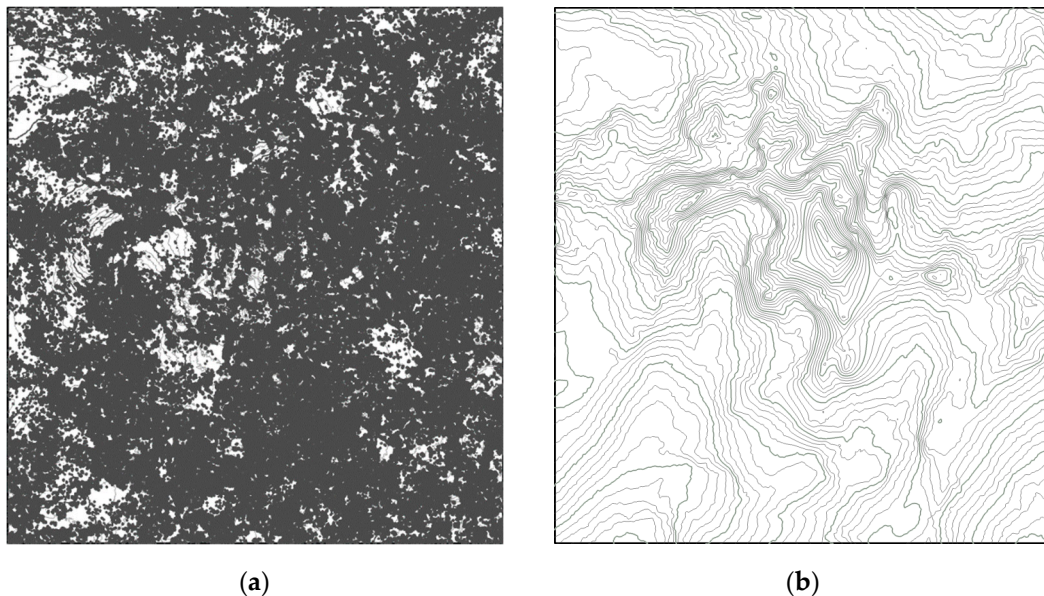


Figure 3. Contour lines (20 m) derived from PLE with different algorithms: (a) SGM (semi-global matching), and (b) ETM (extended terrain matching), which better resolves the features of the mountain summit. The minimum (maximum) elevations using SGM and ETM algorithm are 3168 m (7457 m) and 4204 m (5156 m), respectively. The altitude reference for the highest peak (Batian) is 5199 m.

2.2. The Survey of 2004

In 2004, the last complete glacier inventory of Mt. Kenya was compiled in a map (scale 1:5000) based on aerial photogrammetry [13]. As the original data is unavailable (S. Hastenrath pers. comm.) this map was digitized to derive the glacier extents from 2004, and to serve as a reference for the comparison with Pléiades and Sentinel imagery. As the map coordinates follow the virtual projection established during an early expedition to Mt. Kenya [28], georeferencing to the WGS84 UTM datum was necessary. To achieve this, we used 10 ground control points (GCPs), well distributed over the domain. Four GCPs were surveyed during an earlier study [15] around Lewis Glacier and complemented by field measurements surveyed with a Trimble Receiver R1 (real-time kinematic accuracy 0.7–1.0 m), concurrently to the Pléiades acquisition [29]. All GCPs can be identified in the field as well as in the map, because they represent prominent peaks or boulders, or the color marks, painted for the 2004 airborne survey, which are still visible in the field and depicted in the map. The digitized map was transformed into the WGS84 UTM datum using a spline transformation, which performed well in similar studies [30,31]. The transformation is exact at the GCPs, and no warping was detected.

In the next step, the map contour lines were digitized semi-automatically using the ArcScan extension from ESRI's ArcMap 10.6, and corrected with the topology rules defined in ArcGis Pro 2.1.1 to avoid topological errors. Additionally, 90 elevation points digitized manually from the map complemented the elevation information from the contour lines. Finally, using ArcMap's topo2raster tool, based on the Anudem algorithm [32], all elevation information was interpolated to a hydrologically consistent DEM (ROS) with a cell size of 2 m (Table 2).

2.3. Additional Topographic Data

2.3.1. Sentinel-2 Scene

The Sentinel-2 mission (European Space Agency) consists of two polar orbiting satellites with a phase shift of 180° . The mission provides multispectral images (horizontal resolution for different bands 10/20/60 m) for earth exploring research. Due to a larger number of bands than the Pléiades instrument, it is possible to derive a normalized difference snow and ice index (NDSI) enabling a semi-automatic classification of ice [9]. We used a Sentinel-2A scene (acquired on 15 March 2016, cloud free over the summit region, downloaded from <https://scihub.copernicus.eu/>) to explore the semi-automatic classification of ice as an alternative method of glacier delineation from Pléiades scenes.

2.3.2. TanDEM-X-DEM

The TanDEM-X-DEM (TDX) [33] is a global digital elevation model at ~ 12 m horizontal resolution generated by applying RADAR interferometry from space. TDX access for scientific use was granted by the DLR (German Aerospace Center, TerraSAR-X/TanDEM-X mission) through its call for global data access in 2017. As its horizontal resolution falls between the DEM of the Shuttle Radar Topography Mission (SRTM) or the global DEM of Advanced Spaceborn Thermal Emission and Reflection Radiometer (ASTER GDEM) (~ 30 m) and—usually expensive—very high resolution products, TDX is valuable for various studies depending on high resolution terrain recording [34–36]. TDX constraints are the signal penetration into snow and ice and the time period of acquisition ranging over multiple years. For this study, we focused on the terrain representation of TDX in the same domain as the PLE to focus on the potential of this freely-available TDX product as a tool for monitoring very small glaciers, such as those remaining on Mt. Kenya.

Table 2. Overview of the digital elevation models (DEMs) used in this study.

DEM	Acquisition Method	Cell Size	Acquisition Date
PLE	optical	1 m	23 February 2016
TDX	X-band RADAR	12.32 m	2010–2014
ROS	optical, airborne	2 m	1 September 2004

2.4. Glaciological Analyses

Glacier extents were digitized manually from the 2004 inventory [13], and the 2016 Pléiades orthophoto. Additionally, the NDSI was derived from the Sentinel-2 scene, applying the QGIS semi-automatic classification plugin, to map the glaciers using different thresholds to separate ice from snow and to perform the mapping in shadow areas. Glacier area changes were determined from all glaciers, while glacier volume and mass changes are derived for Lewis Glacier only from differencing the co-registered DEMs [37] of 2010 [12] and 2016 (PLE). The DEM of 2010 was surveyed by differential Global Navigation Satellite System, by crossing the glacier several times, ground controlled by a subset (those surrounding Lewis Glacier) of the same GCPs used for georeferencing the map of 2004 (Section 2.2), and processed to a DEM at 5 m horizontal resolution.

The volume change is derived as the difference of the surface height between the two Lewis Glacier DEMs multiplied by the glacier extent of 2010. To convert volume into mass, a constant ice density of 900 kg/m^3 was assumed. This is justified as the equilibrium line altitude of Lewis has been permanently above the glacier's highest point since the 1990s, causing the loss of the firn area, which leaves a glacier stratigraphy of only ice, with an occasional shallow snow cover of a few centimeters during the rainy seasons [12].

3. Results

3.1. Pleiades Orthophoto

The Pléiades orthophoto and the georeferenced map of 2004 are the primary sources for glacier delineation in this study. With a simple test, we investigate if both products overlap accurately. Assuming that tarn level fluctuations of deeper tarns have little impact on the general shape of the shore line and on the surface area, we consider them as rather stable features for confirming minimal horizontal shifts between both products. We compared the shorelines of 6 tarns around Mt. Kenya summit between the Pléiades orthophoto and the georeferenced map of 2004. The difference of the tarn areas between 2004 and 2016 are below 4% (Figure 4), illustrating good alignment between the products, although the shorelines from 2004 contain a generalization to the map scale of 1:5000. An exception is the shallow and boggy Kami Tarn, where temporal surface area changes due to tarn level fluctuations are very high. Nevertheless, this comparison allows the assessments of glacier area change from the Pléiades orthophoto and the 2004 map to be viewed with confidence.

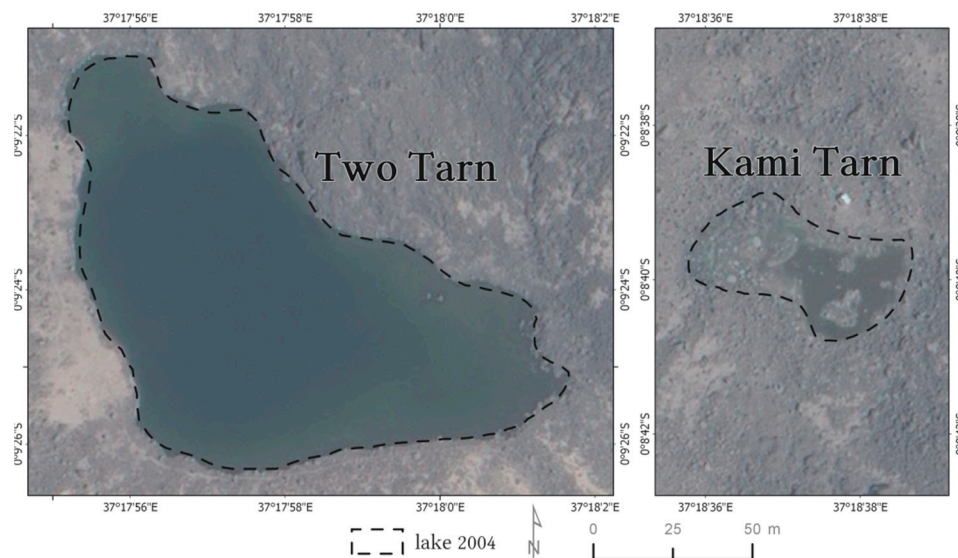


Figure 4. Comparison of the shorelines of two tarns on Mt. Kenya indicating the generally good alignment between the Pléiades orthophoto and the map of 2004, but also one misalignment in the case of shallow Kami Tarn.

3.2. DEM Comparison

We analyzed three different DEMs (Table 2) and compared their horizontal alignment as a relative quality control of the Pléiades processing. For altitude intercomparison, the TDX was corrected for geoid undulation, by reference to mean sea level. The co-registration of the DEMs failed, because the identification of homologous points in the DEMs was not possible, due to the large differences in cell size in each DEM. Thus, our analysis relies upon relative representations of specific surface topography features, like shaded reliefs and catchment divides instead.

Table 3 shows the elevation ranges of the individual DEMs within the ROS domain, and demonstrates the different representations of the lowest and highest pixels. Batian is the highest peak of Mt. Kenya (5199 m), and was used as input elevation point in ROS, and is thus correctly represented. TDX falls short of achieving this maximum summit elevation by 219 m and PLE by 43 m. The minimum elevations are better constrained, where just PLE is 4 m above TDX and ROS.

Errors in steep terrain become visible when plotting the shaded reliefs of the DEMs (Figure 5). Although the timing of PLE acquisition on the late morning coincides with minimum cloud cover and high solar elevation (Table 1), errors due to shadows and distortion still occur in very steep

terrain $> \sim 50^\circ$. TDX errors are flagged by the provided height error map, which is the standard deviation of the random error per pixel due to interferometric decorrelation and incoherence. In the domain, this error is highest over complex terrain characterized by large vertical gradients, and is further the reason for missing the highest peaks (Table 3), if they are built of steep walls instead of gentle slopes (Figure 1). TDX contains corrupted data from artefacts, which introduce completely different terrain properties. While in PLE the ETM algorithm smoothly interpolates errors due to shading of steep walls, TDX falsely introduces different features in the summit region like rough terrain or an expansive flat area (Figure 5). Hence, neither PLE nor TDX result in an acceptable terrain representation for the glacier areas, and TDX is invalid for most of the summit region, and must be rejected for studies demanding a DEM from Mt. Kenya. For the less complex topography of the Lewis Glacier catchment, both products reveal good results, with the constraint that the four year TDX acquisition period averages over the glacier changes that occurred within this period. Hence, for subsequent estimates of glacier volume changes, we use PLE in the Lewis Glacier catchment only.

Table 3. Elevation ranges of different DEMs in the ROS domain.

DEM	Cell Size (m)	Elevation (m)			
		Min	Max	Mean	Std. Deviation
TDX	12.32	4199	4980	4560	153
PLE	1.00	4204	5156	4588	179
ROS	2.00	4199	5199	4592	183

Further, we explored the main ridge lines of the Mt. Kenya summit domain applying ESRI's basin algorithm (without prescribed pour points) as a qualitative measure of confining hydrological catchments (Figure 6). We included SRTM and ASTER DEMs for comparison to widely used datasets. TDX watersheds are rather ill defined, and deviate from the other DEMs due to the large height error in steep terrain (Figure 5). SRTM, ASTER GDEM, ROS, and PLE yield very similar results, although the differences between their cell sizes are large, i.e., ~ 30 m vs. < 2 m. This result indicates that TDX deficiencies in terrain representation are not due to its cell size (~ 12 m), which is coarser than PLE but finer than SRTM or ASTER GDEM.

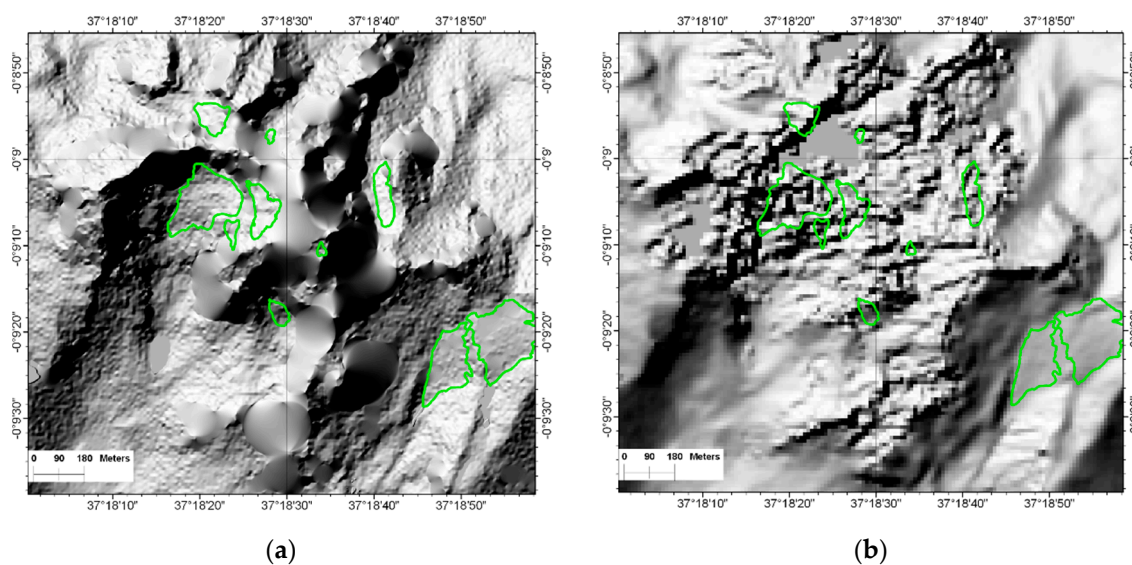


Figure 5. Comparison of the shaded reliefs from (a) PLE and (b) TDX showing errors in steep terrain and glacier outlines from 2016 in green. PLE errors are smoothed and restricted to steep walls, TDX errors are spread over the area with complex terrain, which is interpolated falsely as a rough surface or flat area. Lewis (lower right corner) is the only glacier not affected by DEM interpolation errors.

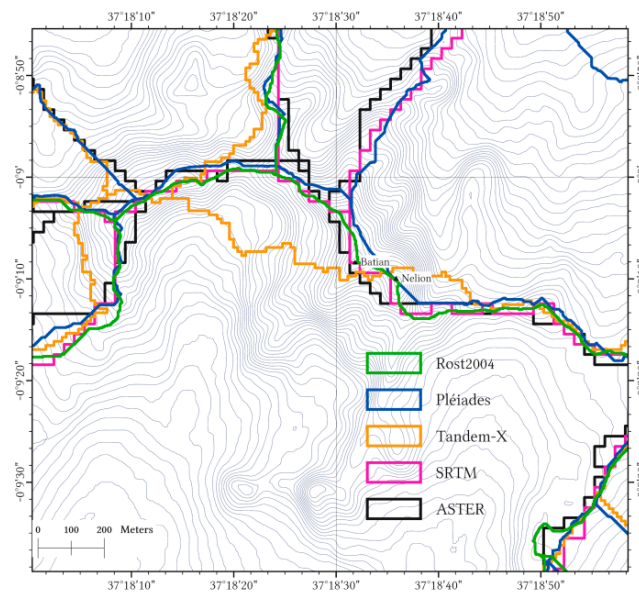


Figure 6. Representation of basin borders derived from the individual DEMs. Contours are taken from the 2004 map (Rost2004). Additionally, basin borders derived from widely used coarser global DEMs (cell size 30 m) SRTM (version 2) and the ASTER (GDEM version 2) are shown (both products are freely available from the U.S. Geological Survey via EarthExplorer (<https://earthexplorer.usgs.gov/>)).

3.3. Glacier Changes

3.3.1. Changes of Glacier Area

The high horizontal resolution of the Pléiades orthophoto and expert knowledge proved to be essential to distinguish the very small glaciers from patches of seasonal snow and to delineate ice from debris or rock in shadow areas. The Sentinel-2 scene was found to be invalid for glacier mapping on Mt. Kenya, because the large errors introduced by its coarser horizontal resolution (20 m) cannot be compensated by finding the best NDSI thresholds for glacier ice detection. However, this result was expected, as this method reaches a limit at glaciers $<0.1 \text{ km}^2$ [9]. Therefore, we confine the mapping to the manual analysis of the Pléiades orthophoto. Throughout the mapping history of the glaciers on Mt. Kenya, the glacier area was defined as the clean ice surface and a potential debris cover was never mapped. Since most glacier margins are well defined by rock walls, debris-covered areas are very limited.

Table 4 shows the glacier area of 2004 and 2016, and the changes that occurred during this period. Glacier retreat is substantial, ranging between the total loss of Gregory (reported earlier in [15]) and a minor area loss of 13% of Forel, a well-shaded hanging glacier. The largest glacier (Lewis) lost 46% of its surface area, which is close to the average loss (44%) of all glaciers on the mountain.

Figure 7 demonstrates the downwasting of Lewis Glacier (see Figure 1 for comparison). The area loss is not only due to terminus retreat, but rather due to shrinkage from all sides, including the separation of the lower from the upper half of the glacier, now divided by a rock outcrop. The glacier surface accumulates sediments washed down from the debris surroundings, which enhance melt by lowering the surface albedo of the glacier [17]. Lewis Glacier area change can be subdivided into two periods, and results in $-28.6 \times 10^3 \text{ m}^2$ (-21% , $-5.2 \times 10^3 \text{ m}^2$ per year) from 2004 to 2010 and in $-34.1 \times 10^3 \text{ m}^2$ (-32% , $-5.7 \times 10^3 \text{ m}^2$ per year) from 2010 to 2016, respectively. Rates of area change slightly increased during the later period, but are still within bounds of the steady shrinkage previously observed over recent decades on Lewis Glacier [12,23].

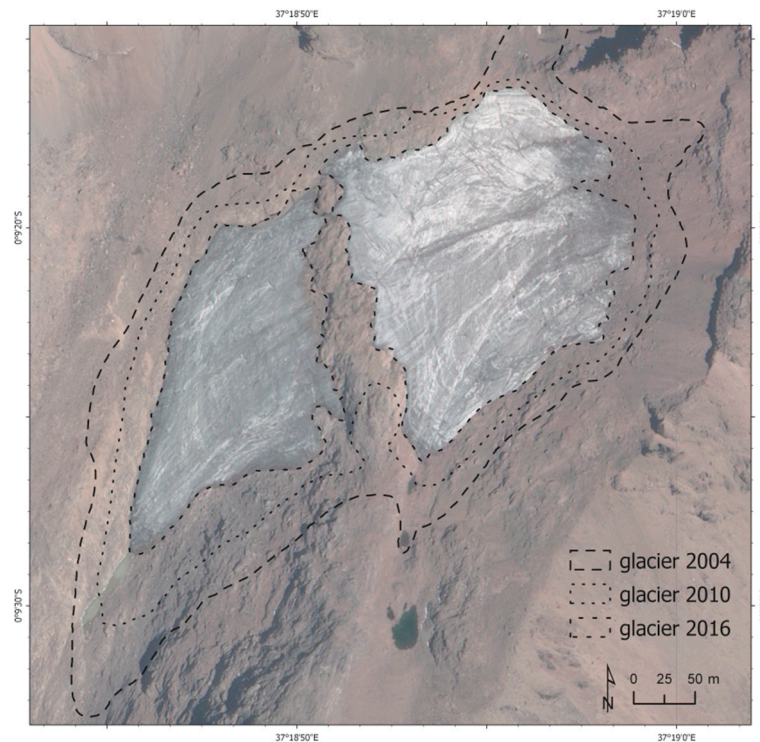


Figure 7. Lewis Glacier seen on the Pléiades orthophoto (pansharpended, nadir) from 23 February 2016. Changes of Lewis Glacier 2004–2016 are depicted by the respective outlines. Former Gregory Glacier, which was still northerly connected to Lewis in 2004, vanished in 2011 [15].

Table 4. Changes of glacier area on Mt. Kenya 2004–2016. Error ranges were derived from horizontal accuracies reported in [13] and this study.

Glacier	Area 2004 (10^3 m^2)	Area 2016 (10^3 m^2)	Difference (10^3 m^2)	Difference (%)
Lewis	136.1 ± 2.2	73.3 ± 3.4	-62.8 ± 1.5	-46
Tyndall	51.7 ± 1.3	38.0 ± 2.4	-13.7 ± 0.4	-26
Krapf	14.9 ± 0.7	12.4 ± 1.4	-2.5 ± 0.1	-17
Forel	12.7 ± 0.7	11.0 ± 1.3	-1.7 ± 0.1	-13
Cesar	18.6 ± 0.8	9.6 ± 1.2	-9.0 ± 0.4	-48
Darwin	12.7 ± 0.7	4.2 ± 0.8	-8.5 ± 0.4	-67
Heim	5.3 ± 0.4	3.0 ± 0.7	-2.3 ± 0.1	-43
Northey	3.9 ± 0.4	1.1 ± 0.4	-2.8 ± 0.2	-72
Diamond	3.1 ± 0.3	1.0 ± 0.4	-2.1 ± 0.2	-68
Gregory	15.6 ± 0.7	0	-15.6	-100
total	274.6 ± 3.1	153.6 ± 5.0	-121.0 ± 2.5	-44

3.3.2. Changes of Glacier Volume

Deriving glacier volume changes from DEM differencing was not carried out for the whole summit domain, as PLE is erroneous in many of the glacier locations, i.e., small cirques below steep walls (Figure 5). However, because the Lewis Glacier catchment is less influenced by steep walls, PLE quality is sufficient for computing volume changes between 2016 and 2010, referring to the previous DEM of Lewis Glacier [12]. We did not calculate volume changes using TDX, because its acquisition period of four years (2010–2014) makes comparisons to the DEMs of 2010 or 2016 doubtful.

PLE was co-registered to the 2010 DEM, and resampled to the same cell size (5 m). DEM differencing showed a volume decrease of $0.89 \times 10^6 \text{ m}^3$ for Lewis Glacier in the period 2010–2016, equivalent to a mass loss of $0.80 \times 10^9 \text{ kg}$, or an annual mass balance rate of -1.47 kg/m^2 (Table 5). Strong negative annual mass balance rates in the 1990s resulted from the loss of the firn body and accompanying

decrease of albedo [12]. The moderate mass loss between 2004 and 2010 is potentially due to very dry conditions, which favor the more energetically demanding ablation process of sublimation over melt [17,38], while the increase of negative mass balance rates since 2010 is caused by decreasing albedo, due to sediment accumulation and increased longwave heating from the surroundings and the recently developed rock outcrops (Figure 7).

Table 5. Volume change and mass balance rate of Lewis Glacier 2004–2016. Values for the period 2004–2010 were taken from [12]. Error ranges were derived from error propagation using horizontal and vertical accuracies from [12,13] and this study.

Year	Volume (106 m ³)	Area (106 m ²)	Period	Mass Balance Rate (kg/m ² /y)
2004	2.37 ± 0.49	0.136 ± 0.007	1993–2004	−2.22 ± 0.44
2010	1.90 ± 0.30	0.107 ± 0.001	2004–2010	−0.63 ± 0.77
2016	1.02 ± 0.34	0.073 ± 0.003	2010–2016	−1.47 ± 0.75

4. Discussion

4.1. Accuracy

On the basis of the rational polynomial coefficients delivered with Pléiades primary data, the root mean square error of the panchromatic nadir orthophoto for the total domain is 8.5 m (circular error in the 90% confidence interval). The acquisition of well distributed GCPs over the total domain was not possible from a cost point of view, and from the acquisition effort. However, 10 recorded off-glacier GCPs in the summit domain (see Section 2.2) were used as control points for validation, yielding a mean absolute horizontal (vertical) error of 3.4 (5.3) m, which is sufficient for the mapping purpose in a scale of 1:25,000, and for delineating glacier extents (Table 4).

For DEM differencing and calculation of glacier volume changes, we followed the advice of earlier publications [8,39] for DEMs constructed without GCPs, and evaluated a vertical bias correction of PLE in the Lewis Glacier catchment. For this, we used the four off-glacier GCPs closely surrounding Lewis from an earlier field campaign [12], which yielded a vertical bias of 0.08 m and a mean absolute error of 1.55 m. Due to the low bias we did not correct PLE but used the error for uncertainty estimates of the volume change (Table 5), by propagating errors from the individual surveys.

As TDX deviates widely from the reference survey (ROS) in the summit domain, a quantitative vertical accuracy estimate was not deemed valuable. The horizontal alignment on flat slopes is acceptable, but for steep slopes in complex terrain, TDX is not an option for cartography and other applications requiring an accurate DEM.

4.2. The Glacier Inventory of 2016

Figure 8 shows the location of the glaciers on Mt. Kenya. Glacier delineation demands high resolution images and expert knowledge, as some of the very small glaciers are located in narrow cirques surrounded by steep walls that cast the glaciers into persistent shadows (Krapf, Cesar, Forel, Heim) or are difficult to distinguish from seasonal snow cover (Northey). Additionally, to the Pléiades orthophoto, we used a Sentinel-2 scene to explore a semi-automatic classification of ice, but due to its coarser resolution and larger shadows, it was impossible to find thresholds for plausible glacier ice detection. Hence, Sentinel-2 is inappropriate for mapping the very small glaciers on Mt. Kenya, and thus, we confirm the interpretation that glaciers <0.1 km² are beyond the limit of detection from platforms like Sentinel-2 or Landsat 8 [9]. This is of potentially wider significance, as receding glacier ice and glacier disintegration means that an increasing proportion of the remaining mountain glaciers of the world become very small, and monitoring these in the future will require the data to meet the same constraints as required presently to map the very small glaciers on Mt. Kenya [40]. Appropriate mapping techniques for very small glaciers may also have increasing significance for providing

accurate information for resolving socioeconomic conflicts over diminishing glacier resources in arid mountainous regions [41].

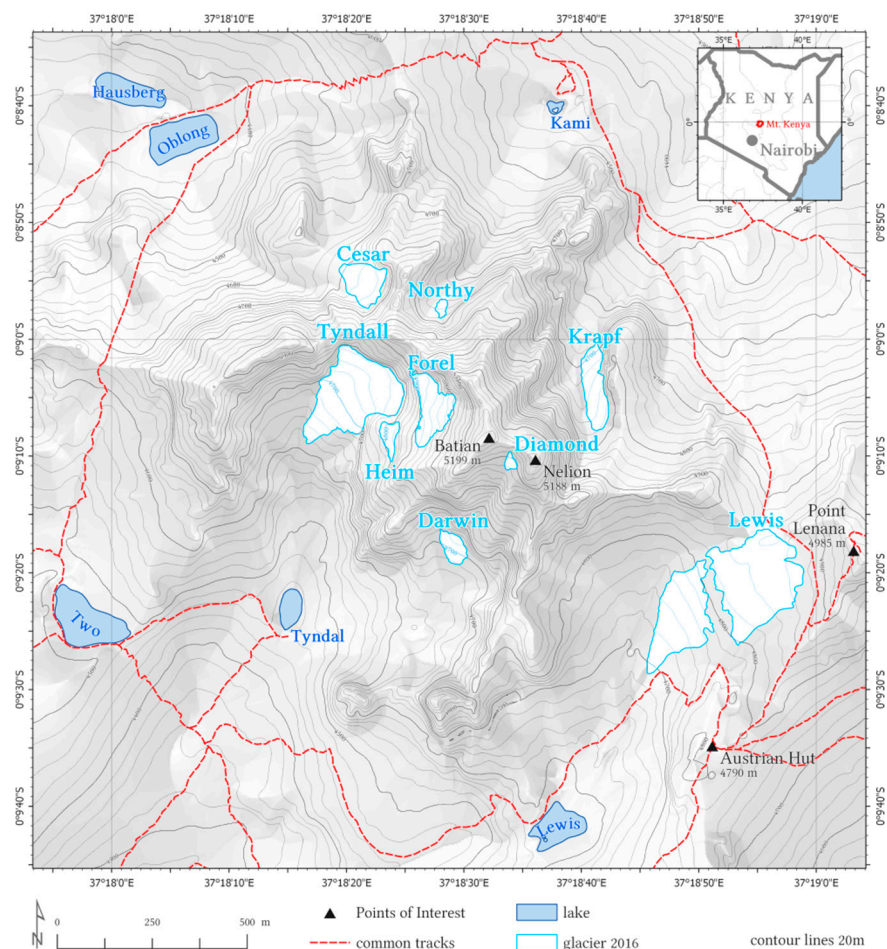


Figure 8. Overview of the glaciers of Mt. Kenya in their 2016 extent.

A major increase of debris cover is not observed on Mt. Kenya's glaciers, unlike in some other mountain regions where glacier retreat is associated with increasing proportions of debris-covered glacier ice [42,43]. Except minor debris deposits from rock fall on Tyndall and Lewis, Mt. Kenya's glaciers remain debris-free. Field observations in periglacial environments adjacent to glaciers or in paraglacial areas of former glacier loss (Gregory) show some geomorphological processes typical of such regimes, but ongoing permafrost degradation due to limited ground snow cover and resulting higher radiation receipts [44] is in line with a general decay of the cryosphere in the summit region.

In total, the glacier area on Mt. Kenya decreased from $274.6 \times 10^3 \text{ m}^2$ to $153.0 \times 10^3 \text{ m}^2$ (−44%), from 2004 to 2016. This is in line with data from nearby Kilimanjaro [45] and tropical South America [46], indicating tropical glacier retreat is stronger than the global mean. Absolute annual retreat rates on Mt. Kenya have been rather constant, between $10 \times 10^3 \text{ m}^2$ and $13 \times 10^3 \text{ m}^2$ per year over the last 50 years. Corresponding relative annual retreat rates increased from 0.8% per year (1947–1963) to 3.2% per year (1993–2004) [14], and currently reach 3.8% (2004–2016). Global estimates for future glacier mass loss suggest that the preservation of glaciers by ambitious measures is possible in the long term [47]. However, if current retreat rates prevail, Mt. Kenya's glaciers will vanish before 2030. Linear extrapolations of the rates of volume change of Lewis will result in the extinction

of the glacier before 2025, leaving a void in tropical glaciology studies and their importance for understanding the climatology of low latitudes [48].

5. Conclusions

This study explores the practicability of DEMs from Pléiades (PLE) and TanDEM-X (TDX) for monitoring very small glaciers in complex terrain. PLE was generated without ground control for a different purpose (topographic mapping), and its use in a smaller domain is found to be sufficient for glacier delineating and calculation of glacier volume change. On Mt. Kenya, the benefits of new and highly appreciated techniques (high spatial and temporal resolution, free data access, well documented procedures) like glacier mapping from Sentinel-2 or surface height change detection from TDX, reach their limit of feature identification. Therefore, monitoring of very small glaciers demands products of highest spatial resolution (e.g., Pléiades images), counterbalanced by the acquisition costs of such products.

The updated glacier inventory of Mt. Kenya demonstrates a persisting glacier retreat at constant pace for glacier area changes and increased mass loss rates, resulting in the projected complete deglaciation of the massif by the end of the next decade. The extinction of Mt. Kenya's glaciers connotes the cessation of the longest time series of glacier monitoring in the tropics.

Author Contributions: R.P. developed the storyline, wrote the paper, and performed the glaciological analysis. M.L. and A.H. focused on the Pléiades analysis, the DEM generation and comparison, and the GIS methods. L.I.N. and G.K. contributed to the glaciological analysis and helped to refine the storyline and the English.

Funding: This research was funded by the FFG (Austrian Research Promotion Agency) grant number 4948512. Additionally, the authors acknowledge the financial support by the University of Graz.

Acknowledgments: We acknowledge the DLR (German Aerospace Center) for providing the TanDEM-X-DEM data (grant: DEM_GLAC1560) acquired by the TerraSAR-X/TanDEM-X satellite. Thanks are due to the reviewers for their valuable and constructive comments.

Conflicts of Interest: The authors declare no conflict of interest.

References

1. Marzeion, B.; Champollion, N.; Haerberli, W.; Langley, K.; Leclercq, P.; Paul, F. Observation-Based Estimates of Global Glacier Mass Change and Its Contribution to Sea-Level Change. *Surv. Geophys.* **2017**, *38*, 105–130. [[CrossRef](#)] [[PubMed](#)]
2. UNEP. *WGMS Global Glacier Changes: Facts and Figures*; UNEP: Nairobi, Kenya, 2008.
3. Haerberli, W.; Cihlar, J.; Barry, R.G. Glacier monitoring within the Global Climate Observing System. *Ann. Glaciol.* **2000**, *31*, 241–246. [[CrossRef](#)]
4. Zemp, M.; Frey, H.; Gärtner-Roer, I.; Nussbaumer, S.U.; Hoelzle, M.; Paul, F.; Haerberli, W.; Denzinger, F.; Ahlström, A.P.; Anderson, B.; et al. Historically unprecedented global glacier decline in the early 21st century. *J. Glaciol.* **2015**, *61*, 745–762. [[CrossRef](#)]
5. Paul, F. Rapid disintegration of Alpine glaciers observed with satellite data. *Geophys. Res. Lett.* **2004**, *31*, L21402. [[CrossRef](#)]
6. Zemp, M.; Armstrong, R.; Gärtner-Roer, I.; Haerberli, W.; Hoelzle, M.; Käab, A.; Kargel, J.S.; Khalsa, S.J.S.; Leonard, G.J.; Paul, F.; et al. Global glacier monitoring—A long-term task integrating in situ observations and remote sensing. In *Global Land Ice Measurements from Space*; Kargel, J.S., Leonard, G.J., Bishop, M.P., Käab, A., Raup, B.H., Eds.; Springer Verlag: Berlin/Heidelberg, Germany, 2014; p. 876.
7. Paul, F.; Käab, A.; Haerberli, W. Recent glacier changes in the Alps observed by satellite: Consequences for future monitoring strategies. *Glob. Planet. Chang.* **2007**, *56*, 111–122. [[CrossRef](#)]
8. Paul, F.; Bolch, T.; Käab, A.; Nagler, T.; Nuth, C.; Scharrer, K.; Shepherd, A.; Strozzi, T.; Ticconi, F.; Bhambri, R.; et al. The glaciers climate change initiative: Methods for creating glacier area, elevation change and velocity products. *Remote Sens. Environ.* **2015**, *162*, 408–426. [[CrossRef](#)]
9. Paul, F.; Winsvold, S.; Käab, A.; Nagler, T.; Schwaizer, G. Glacier Remote Sensing Using Sentinel-2. Part II: Mapping Glacier Extents and Surface Facies, and Comparison to Landsat 8. *Remote Sens.* **2016**, *8*, 575. [[CrossRef](#)]

10. Hastenrath, S. *The Glaciers of Equatorial East Africa*; D. Reidel Publishing Company: Dordrecht, The Netherlands; Boston, MA, USA; Lancaster, UK, 1984.
11. Hastenrath, S. *Glaciological Studies on Mount Kenya*; University of Wisconsin-Madison: Madison, WI, USA, 2005.
12. Prinz, R.; Fischer, A.; Nicholson, L.; Kaser, G. Seventy-six years of mean mass balance rates derived from recent and re-evaluated ice volume measurements on tropical Lewis Glacier, Mount Kenya. *Geophys. Res. Lett.* **2011**, *38*, L20502. [[CrossRef](#)]
13. Rostom, R.S.; Hastenrath, S. Variations of Mount Kenya's glaciers 1993–2004. *Erdkunde* **2007**, *61*, 277–283. [[CrossRef](#)]
14. Hastenrath, S. The glaciers of Mount Kenya 1899–2004. *Erdkunde* **2005**, *59*, 120–125. [[CrossRef](#)]
15. Prinz, R.; Nicholson, L.; Kaser, G. Variations of the Lewis Glacier, Mount Kenya, 2004–2012. *Erdkunde* **2012**, *66*, 255–262. [[CrossRef](#)]
16. Prinz, R. Lewis Glacier, Mount Kenya, 2010 (1:2500). In *Fluctuations of Glaciers 2005–2010, Volume X*; Zemp, M., Frey, H., Gärtner-Roer, I., Nussbaumer, S.U., Hoelzle, M., Paul, F., Haeberli, W., Eds.; World Glacier Monitoring Service: Zürich, Switzerland, 2012; p. 66.
17. Prinz, R.; Nicholson, L.; Mölg, T.; Gurgiser, W.; Kaser, G. Climatic controls and climate proxy potential of Lewis Glacier, Mt. Kenya. *Cryosphere* **2016**, *10*, 133–148. [[CrossRef](#)]
18. Francou, B.; Vuille, M.; Wagnon, P.; Mendoza, J.; Sicart, J.E. Tropical climate change recorded by a glacier in the central Andes during the last decades of the twentieth century: Chacaltaya, Bolivia, 16° S. *J. Geophys. Res.* **2003**, *108*, 4154. [[CrossRef](#)]
19. Vuille, M.; Francou, B.; Wagnon, P.; Juen, I.; Kaser, G.; Mark, B.; Bradley, R.S. Climate change and tropical Andean glaciers: Past, present and future. *Earth-Sci. Rev.* **2008**, *89*, 79–96. [[CrossRef](#)]
20. Mölg, T.; Cullen, N.J.; Hardy, D.R.; Winkler, M.; Kaser, G. Quantifying climate change in the tropical midtroposphere over East Africa from glacier shrinkage on Kilimanjaro. *J. Clim.* **2009**, *22*, 4162–4181. [[CrossRef](#)]
21. Karl, T.R.; Hassol, S.J.; Miller, C.D.; Murray, W.L. *Temperature Trends in the Lower Atmosphere: Steps for Understanding and Reconciling Differences*; General Books LLC: Washington, DC, USA, 2006.
22. Pepin, N.C.; Lundquist, J.D. Temperature trends at high elevations: Patterns across the globe. *Geophys. Res. Lett.* **2008**, *35*, 1–6. [[CrossRef](#)]
23. Mölg, T.; Cullen, N.J.; Hardy, D.R.; Kaser, G.; Nicholson, L.; Prinz, R.; Winkler, M. East African glacier loss and climate change: Corrections to the UNEP article “Africa without ice and snow”. *Environ. Dev.* **2013**, *6*, 1–6. [[CrossRef](#)]
24. WGMS. *Global Glacier Change Bulletin No. 2 (2014–2015)*; Zemp, M., Nussbaumer, S.U., Gärtner-Roer, I., Huber, J., Machguth, H., Paul, F., Hoelzle, M., Eds.; ICSU(WDS)/IUGG(IACS)/UNEP/UNESCO/WMO; World Glacier Monitoring Service: Zurich, Switzerland, 2017.
25. Nicholson, L. Photographs of Lewis Glacier Change 2003–2014. Available online: <http://lindseynicholson.org/2014/10/photographs-of-lewis-glacier-change-2003-2014/> (accessed on 20 March 2018).
26. Hirschmüller, H. Accurate and efficient stereo processing by semi-global matching and mutual information. In Proceedings of the 2005 IEEE Computer Society Conference on Computer Vision and Pattern Recognition (CVPR'05), San Diego, CA, USA, 20–25 June 2005; Volume 2, pp. 807–814.
27. Harris, C.; Stephens, M. A combined corner and edge detector. *Proc. Alvey Vis. Conf.* **1988**, *15*, 147–151.
28. Charnley, F.E. Some observations on the glaciers of Mount Kenya. *J. Glaciol.* **1959**, *3*, 483–492. [[CrossRef](#)]
29. Ladner, M.; Heller, A.; Grillmayer, E. GNSS und Pléiades-Bilder in der Hochgebirgskartographie. *AGIT J. Angew. Geoinform.* **2017**, *3*, 13–23.
30. Heller, A. Die Alpenvereinskarte als Grundlage für Geographische Informationssysteme. *Wiss. Alpenvereinshefte* **2001**, *34*, 61–81.
31. Heller, A. Georeferenzierung von Alpenvereinskarten mit radialen Basisfunktionen. In *Angewandte Geographische Informationsverarbeitung XIV*; Strobl, J., Blaschke, T., Griesebener, G., Eds.; AGIT: Salzburg, Austria, 2002; pp. 162–171.
32. Hutchinson, M.F. A new procedure for gridding elevation and stream line data with automatic removal of spurious pits. *J. Hydrol.* **1989**, *106*, 211–232. [[CrossRef](#)]
33. Wessel, B. *TanDEM-X Ground Segment DEM Products Specification Document*; Public Document TD-GS-PS-0021, Issue 3.1; EOC, DLR: Oberpfaffenhofen, Germany, 2016.

34. Rankl, M.; Braun, M. Glacier elevation and mass changes over the central Karakoram region estimated from TanDEM-X and SRTM/X-SAR digital elevation models. *Ann. Glaciol.* **2016**, *57*, 273–281. [[CrossRef](#)]
35. Rott, H.; Floricioiu, D.; Wuite, J.; Scheiblaue, S.; Nagler, T.; Kern, M. Mass changes of outlet glaciers along the Nordenskjöld Coast, northern Antarctic Peninsula, based on TanDEM-X satellite measurements. *Geophys. Res. Lett.* **2014**, *41*, 8123–8129. [[CrossRef](#)]
36. Pipaud, I.; Loibl, D.; Lehmkühl, F. Evaluation of TanDEM-X elevation data for geomorphological mapping and interpretation in high mountain environments—A case study from SE Tibet, China. *Geomorphology* **2015**, *246*, 232–254. [[CrossRef](#)]
37. Klug, C.; Bollmann, E.; Galos, S.P.; Nicholson, L.; Prinz, R.; Rieg, L.; Sailer, R.; Stötter, J.; Kaser, G. Geodetic reanalysis of annual glaciological mass balances (2001–2011) of Hintereisferner, Austria. *Cryosphere* **2018**, *12*, 833–849. [[CrossRef](#)]
38. Hastenrath, S.; Polzin, D.; Mutai, C. Diagnosing the droughts and floods in Equatorial East Africa during boreal autumn 2005–08. *J. Clim.* **2010**, *23*, 813–817. [[CrossRef](#)]
39. Berthier, E.; Vincent, C.; Magnússon, E.; Gunnlaugsson, Á.Þ.; Pitte, P.; Le Meur, E.; Masiokas, M.; Ruiz, L.; Pálsson, F.; Belart, J.M.C.; et al. Glacier topography and elevation changes derived from Pléiades sub-meter stereo images. *Cryosphere* **2014**, *8*, 2275–2291. [[CrossRef](#)]
40. Fischer, M.; Huss, M.; Barboux, C.; Hoelzle, M. The New Swiss Glacier Inventory SGI2010: Relevance of Using High-Resolution Source Data in Areas Dominated by Very Small Glaciers. *Arct. Antarct. Alp. Res.* **2014**, *46*, 933–945. [[CrossRef](#)]
41. Nicholson, L.; Marín, J.; Lopez, D.; Rabatel, A.; Bown, F.; Rivera, A. Glacier inventory of the upper Huasco valley, Norte Chico, Chile: Glacier characteristics, glacier change and comparison with central Chile. *Ann. Glaciol.* **2009**, *50*, 111–118. [[CrossRef](#)]
42. Stokes, C.R.; Popovnin, V.; Aleynikov, A.; Gurney, S.D.; Shahgedanova, M. Recent glacier retreat in the Caucasus Mountains, Russia, and associated increase in supraglacial debris cover and supra-/proglacial lake development. *Ann. Glaciol.* **2007**, *46*, 195–203. [[CrossRef](#)]
43. Shukla, A.; Gupta, R.P.; Arora, M.K. Estimation of debris cover and its temporal variation using optical satellite sensor data: A case study in Chenab basin, Himalaya. *J. Glaciol.* **2009**, *55*, 444–452. [[CrossRef](#)]
44. Grab, S.W.; Gatebe, C.K.; Kinyua, A.M. Ground thermal profiles from Mount Kenya, East Africa. *Geogr. Ann. Ser. A Phys. Geogr.* **2004**, *86*, 131–141. [[CrossRef](#)]
45. Cullen, N.J.; Sirguey, P.; Mölg, T.; Kaser, G.; Winkler, M.; Fitzsimons, S.J. A century of ice retreat on Kilimanjaro: The mapping reloaded. *Cryosphere* **2013**, *7*, 419–431. [[CrossRef](#)]
46. Rabatel, A.; Francou, B.; Soruco, A.; Gomez, J.; Cáceres, B.; Ceballos, J.L.; Basantes, R.; Vuille, M.; Sicart, J.E.; Huggel, C.; et al. Current state of glaciers in the tropical Andes: A multi-century perspective on glacier evolution and climate change. *Cryosphere* **2013**, *7*, 81–102. [[CrossRef](#)]
47. Marzeion, B.; Kaser, G.; Maussion, F.; Champollion, N. Mass loss commitment limits influence of climate change mitigation on glaciers. *Nat. Clim. Chang.* **2018**. online first. [[CrossRef](#)]
48. Kaser, G. Glacier-climate interaction at low latitudes. *J. Glaciol.* **2001**, *47*, 195–204. [[CrossRef](#)]

